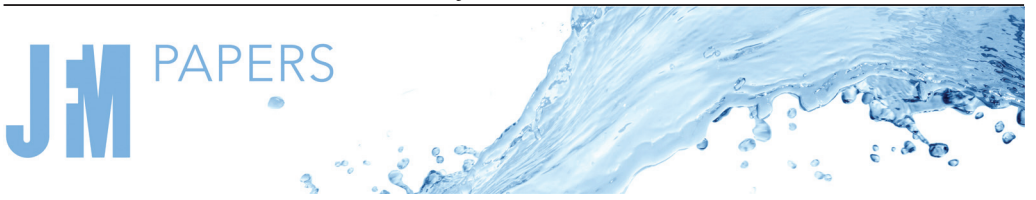
J. Fluid Mech. (2022), *vol*. 948, A19, doi:10.1017/jfm.2022.649



Phase diagram for preferential flow in dual permeable media

Fanli Liu[1] **and Moran Wang**[1],†

[1]Department of Engineering Mechanics, Tsinghua University, Beijing 100084, PR China

(Received 17 March 2022; revised 30 June 2022; accepted 18 July 2022)

We study the preference of two-phase displacements systematically by theoretical derivations and numerical simulations via a non-uniform pore doublet model. All the most important impact factors, including viscosity ratio, capillary number, wetting conditions and boundary conditions, have been considered, and finally a complete phase diagram for preferential flow has been obtained. The simple treatment for the dual-permeability media has been validated, and further, with a few necessary corrections the phase diagram is applicable for disordered permeable media in general. These results help us to understand the occurrence and manipulation of preferential flow in heterogeneous permeable media.

Key words: porous media

1. Introduction

Preferential flow refers to the non-uniform flow pattern in disordered media where certain flow pathways are more favoured than others, usually during two-phase displacement. Its occurrence is ubiquitous in nature and many fields of industry, including enhanced oil recovery, soil wetting, carbon dioxide storage and drug delivery (Huppert & Neufeld 2014; Good, Noone & Bowen 2015; Odier *et al.* 2017; Jensen & Chernyavsky 2019). Extensive studies have long been carried out on the preferential flow in homogeneous media (Lenormand & Zarcone 1985; Cieplak & Robbins 1988), and a well-known phase diagram illustrating the impact of viscosity ratio λ and capillary number Ca on flow patterns has been obtained and verified by multiple works (Lenormand, Touboul & Zarcone 1988; Ferer *et al.* 2004; Cottin, Bodiguel & Colin 2010; Zhang *et al.* 2011). We define λ as the viscosity ratio of invading to defending fluid, and $Ca = \mu v/\sigma$ describes the ratio of viscous force to capillary force, with μ being the viscosity, v the velocity, and σ the interfacial tension. High Ca and large λ both tend to stabilize the displacing front (Aker, Måløy & Hansen 2000), whereas preferential flow occurs due to capillary fingering at low Ca or due to viscous fingering at low λ (Måløy, Feder & Jøssang 1985;

† Email address for correspondence: mrwang@tsinghua.edu.cn

© Tsinghua University, 2022. Published by Cambridge University Press

https://doi.org/10.1017/jfm.2022.649 Published online by Cambridge University Press

Babchin *et al.* 2008). In recent years, researchers have expanded the existing knowledge of preferential flow in homogeneous media to include the impact of wetting conditions and three-dimensional layer flows (Holtzman & Segre 2015; Trojer, Szulczewski & Juanes 2015; Primkulov *et al.* 2021).

In contrast, there is some lack of knowledge of the preferential flow in heterogeneous media. Researchers have studied the preferential flow as an interface instability (fingering) in randomly heterogeneous media (Chen & Neuman 1996; Tartakovsky, Neuman & Lenhard 2003; Oliveira *et al.* 2006), but another kind of preferential flow can be much more dominant, in media with specific types of heterogeneity, than fingerings in homogeneous or randomly heterogeneous media. One common type of such heterogeneity is the difference in permeability between layers in a permeable medium, usually encountered in the underground condition (Phillips 2009; Hewitt, Neufeld & Lister 2014; Bahadori 2018). A pore doublet model, which consists of two channels of unequal radii, was often adopted to represent the layered feature (Moore & Slobod 1955). Early results from the pore doublet model indicated that the phase diagram obtained from the homogeneous case was no longer applicable (Chatzis & Dullien 1983). However, all factors, including the viscosity ratio, capillary number and wetting condition, impact the preferential flow so that most of the previous studies were limited to some special cases and thus hardly yielded a new general phase diagram (Moore & Slobod 1955; Chatzis & Dullien 1983; Sorbie, Wu & McDougall 1995; Al-Housseiny, Hernandez & Stone 2014; Khayamyan, Lundström & Gustavsson 2014; Zheng *et al.* 2018). In addition, although either pressure or velocity inlet boundary has been considered in previous studies, the difference between the boundary conditions, and the impact of the boundary conditions have been rarely investigated. One recent work obtained a λ–Ca relation for the simultaneous arrival in a pore doublet model at a fixed water-wet contact angle (for simplicity, the invading and defending fluids are referred to as water and oil) and a constant inlet velocity (Gu, Liu & Wu 2021). In this work, we are to produce a complete phase diagram for the preferential flow in a pore doublet, which will include the impacts of viscosity ratio, capillary number, wetting conditions and boundary conditions. We further demonstrate how the phase diagram from the pore doublet can be extended to the dual permeable media in general.

2. Methods

The two-dimensional pore doublet model in figure 1(*a*) is adopted in this work. We use a curved shape to prevent sharp turns in a straight channel from altering the local interface curvature. The inner circle is large enough so that the lengths of the channels are identical. Assuming a steady laminar flow, we have the governing equations $\Delta p = (3q_k/2r_k^3)[\mu_w L_k + \mu_o(L - L_k)] - \sigma\cos\theta/r_k$ and $\Delta p = (3q_1/2r_1^3)[\mu_w L_1 + \mu_o(L - L_1)] - \sigma\cos\theta/r_1$. Here, Δp is the external pressure difference over the channel; q_1, r_1 and L_1 are, respectively, the flux, the radius and the displaced length in the wider channel, while q_k, $r_k = kr_1$ $(k < 1)$ and L_k are those in the other channel; L is the full length of the channel; θ is the contact angle; and μ_w and μ_o are the viscosities of water and oil. By defining $q_1 = 2r_1 v_1 = 2r_1\,\mathrm{d}L_1/\mathrm{d}t$, with v_1 being the velocity of the interface, the governing equations can be solved numerically given the boundary condition. The same two-phase displacement process can also be solved by the lattice Boltzmann method (LBM) (Liu & Wang 2022*a*), a brief introduction to which is given in Appendix A. The following results for the pore doublet model are obtained by both solving the differential equations and the LBM, which agree with one another. We are

https://doi.org/10.1017/jfm.2022.649 Published online by Cambridge University Press

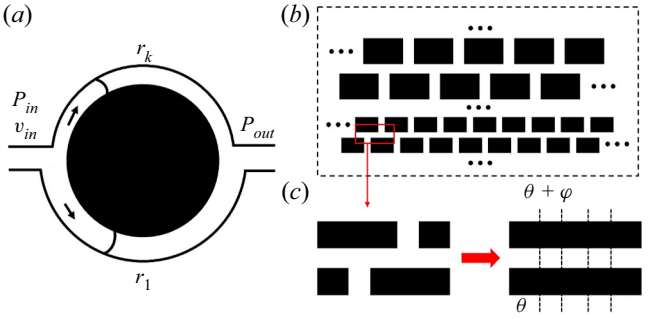


Figure 1. (*a*) The pore doublet model in this work. (*b*) Diagram of the dual-permeability media studied in this work. (*c*) A simple treatment that reduces the converging–diverging feature of porous media to an alternating pattern of heterogeneous contact angles. The diverging throat–pore junction is simplified to part of a straight channel with contact angle altered to $\theta + \varphi$ from the intrinsic value θ.

particularly interested in the displacement ratio α_k that characterizes the preferential flow, defined as L_k/L_1 at breakthrough. It can be understood as the dominance of the narrow channel, with $\alpha_k = 1$ corresponding to simultaneous displacement in both channels.

The analyses in a dual-permeability medium are much more complex, so few relevant studies have been reported in the literature. Apart from solving directly the two-phase displacement in permeable media as in figure 1(*b*) with the LBM, we propose a simple treatment that allows us to solve numerically the differential equations similar to those of the pore doublet model. Since our focus is on the preferential flow in the horizontal direction, the essential difference is that the porous medium usually has the inevitable converging–diverging feature (Payatakes 1982). This feature leads to changes of the interfacial curvature at the converging–diverging spots, namely the pore–throat junctions. We simplify the changes of local interfacial curvature to the local wettability alteration (Liu & Wang 2022*b*), and thus we reduce the dual-permeability medium to a pore doublet with heterogeneous contact angles θ and $\theta + \varphi$ in a periodically alternating pattern, illustrated in figure 1(*c*). We adopt the model where $\varphi = 45^\circ$ and the percentage of $\theta + \varphi$ in length is 0.2, since the pore–throat junctions usually make up a shorter length compared to the path inside pores and throats. We have done a quantitative validation of the simple treatment. For $\theta = 60^\circ$, we solve for α_k in the permeable media in figure 1(*b*) by the LBM, and compare the result with the simple model. Good agreements have been found when φ is set to be 33°. The exact value of φ is dependent on the local pore–throat structure and the flow conditions, thus it is not easy to determine, but the idea of treating the converging–diverging feature as an alternating pattern of contact angles should be universal.

The values of the parameters have been validated to not affect the qualitative findings, which indicates that our findings apply to the dual media in both small and large scales. For the pore doublet case, $L = 1500\ \mu\text{m}$, $r_1 = 37.5\ \mu\text{m}$, $k = 2/3$, $r_k = 25\ \mu\text{m}$, $\mu_o = 10^{-3}$ Pa s and $\sigma = 0.02$ N m^{-1}. For the porous media, the size of the structure itself is 535×680 in lattice units with grid width $\Delta x = 2.5 \times 10^{-6}$ m, and we add two buffer layers of 20 grids at the inlet and outlet.

3. Results and discussion

We emphasize the impact of boundary condition before presenting the results. The pressure and velocity inlet are equivalent only when both the capillary and viscous

https://doi.org/10.1017/jfm.2022.649 Published online by Cambridge University Press

resistance are constant during the displacement. Otherwise, the inlet pressure being constant means that the inlet velocity changes during displacement, and vice versa. Consequently, we define the capillary number based on the boundary condition. For the velocity inlet we have $Ca_v = \mu_o q/(2\sigma\cos\theta r_1)$, and for the pressure inlet we have $Ca_p = \Delta p/(\sigma\cos\theta/r_1)$, where q is the total flux. Here, Ca_v and Ca_p can be understood as dimensionless velocity and pressure, respectively (Guo, Song & Hilfer 2020).

When $\lambda = \mu_w/\mu_o = 1$, the two boundary conditions are equivalent in a pore doublet, and we obtain the analytical α_k–Ca_p relation as $\alpha_k|_{\lambda=1} = k^2[(k^{-1}-1)/(1+Ca_p)+1]$. This simple case provides useful insights for the impact of Ca (Ca_v and Ca_p) and wettability in general. The behaviour of preferential flow depends on the wetting state being water-wet or oil-wet, but not on the specific contact angle at any given capillary number. All oil-wet conditions show the same α_k–Ca_p curve, and similarly for all water-wet conditions. Under an oil-wet condition, the range of Ca_p is $(-\infty, -k^{-1})$ to allow flow in both channels. Because the capillary resistance is higher in the narrow channel, the wide channel dominates the flow ($\alpha_k \to 0$) as $Ca_p \to -k^{-1}$. Then α_k increases monotonically with increasing external pressure or velocity, and is bounded by $\alpha_k = k^2$ as $Ca_p \to -\infty$. For a water-wet condition, the range of Ca_p is $(-1, \infty)$. The capillary driving force is weaker in the wide channel, so the narrow channel dominates the flow ($\alpha_k \to \infty$) when the external driving pressure is the smallest as $Ca_p \to -1$. Here, the external pressure is a resistance force that cancels out the capillary driving force in the wide channel. Then α_k decreases monotonically with increasing Ca_p, and is also bounded by $\alpha_k = k^2$ as $Ca_p \to \infty$. An immediate deduction is that in the same doublet, α_k is always lower in oil-wet conditions than in water-wet conditions. Spontaneous imbibition leads to preferential flow in the wide channel ($\alpha_k = k$), and simultaneous arrival can occur only when the pressure difference is negative in water-wet conditions.

With varying λ, the two boundary conditions are no longer equivalent. Under a pressure inlet, the α_k–Ca_p relations at different λ are shown in figures 2(*a*,*b*). The range of Ca_p and the point of simultaneous arrival remain the same regardless of λ. Compared to the $\lambda = 1$ curve, $\lambda < 1$ will strengthen the preferential flow no matter which channel dominates, making the whole curve deviate from $\alpha_k = 1$. On the other hand, $\lambda > 1$ will shift the curve closer to $\alpha_k = 1$ and suppress the preferential flow. The impact of λ at $\lambda < 1$ is similar to the viscous fingering effect (Måløy *et al.* 1985), and that at $\lambda > 1$ is similar to the viscous stabilizing effect in homogeneous media (Aker *et al.* 2000). Yet in homogeneous media, a large enough λ will lead to a fully stable displacing front and prevent the preferential flow (Lenormand *et al.* 1988; Zhang *et al.* 2011). In the pore doublet, however, we can derive theoretically and validate that the ability of λ to shift the α_k–Ca_p relation has a limit. As $\lambda \to 0$, $\alpha_k|_{\lambda\to 0} \to 1 - \sqrt{1-\alpha_k|_{\lambda=1}}$ if $\alpha_k|_{\lambda=1} \le 1$, and $\alpha_k|_{\lambda\to 0} \to \left(1 - \sqrt{1-(\alpha_k|_{\lambda=1})^{-1}}\right)^{-1}$ if $\alpha_k|_{\lambda=1} > 1$. As $\lambda \to \infty$, $\alpha_k|_{\lambda\to\infty} = \sqrt{\alpha_k|_{\lambda=1}}$. In other words, a large λ can at most reduce the preferential flow from $\alpha_k|_{\lambda=1}$ to $\sqrt{\alpha_k|_{\lambda=1}}$. The previous observations on the impact of Ca and wetting conditions when $\lambda = 1$ remain mostly true.

The phase diagram under a pressure inlet is given in figures 3(*a*,*b*). The curve of simultaneous arrival ($\alpha_k = 1$) is a straight line parallel to the $\log(\lambda)$ axis. This implies that the state of preferential flow under a constant boundary condition is determined primarily by Ca_p, or the dimensionless pressure difference. The slope of any curve turns flat as λ becomes very large or small, indicating that α_k converges at a large enough or small enough λ, as we have observed from the α_k–Ca_p curves.

https://doi.org/10.1017/jfm.2022.649 Published online by Cambridge University Press

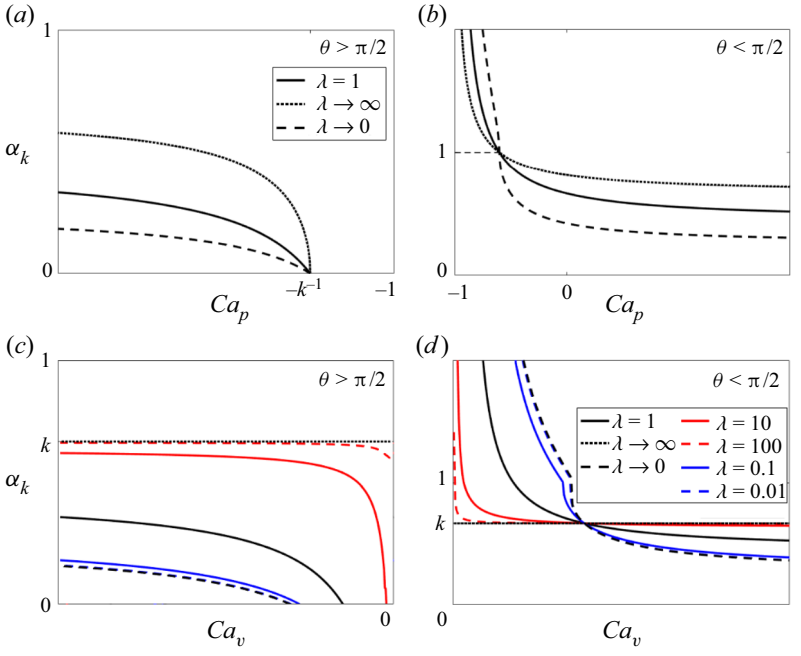


Figure 2. The α_k–Ca (Ca_p or Ca_v) relation with varying λ in the pore doublet: (*a*) under a pressure inlet at $\theta > \pi/2$; (*b*) under a pressure inlet at $\theta < \pi/2$; (*c*) under avelocity inlet at $\theta > \pi/2$; (*d*) under a velocity inlet at $\theta < \pi/2$. The point of simultaneous arrival is an invariant point under a pressure inlet, while under avelocity inlet, the invariant point is the point of spontaneous imbibition. The impact of λ is bounded by the $\lambda \to 0$ and $\lambda \to \infty$ curves.

We then consider the velocity inlet boundary. The α_k–Ca_v relation at different λ in figures 2(*c*,*d*) also shows an invariant point, but it is at the spontaneous imbibition point where $\alpha_k|_{\lambda=1} = k$, not the simultaneous arrival point under a pressure inlet. Consequently, $\lambda < 1$ shifts the curve away from $\alpha_k = k$ instead of $\alpha_k = 1$, and $\lambda > 1$ shifts the curve towards $\alpha_k = k$. This invariant point can be understood as follows. Assume that the displaced length in each channel increases by ΔL_1 and ΔL_k in one time step. Then the consequent change of Δp in each channel will be $3q_1(\mu_o - \mu_w)\,\Delta L_1/(2{r_1}^3)$ and $3q_k(\mu_o - \mu_w)\,\Delta L_k/(2{r_k}^3)$. If α_k is to be kept unchanged, then the flux in each channel should also be unchanged, and equating the previous two expressions yields $v_k/v_1 = k$. Now the impact of λ on preferential flow is more complex and depends on which of the three intervals $\alpha_k|_{\lambda=1}$ falls in: $(0, k]$, $(k, 1)$ or $[1, \infty)$. For example, a larger λ shifts the curve towards $\alpha_k = k$, so it suppresses the preferential flow when $\alpha_k|_{\lambda=1} \in (0, k]$ or $[1, \infty)$, but strengthens the preferential flow when $\alpha_k|_{\lambda=1} \in (k, 1)$. As λ decreases, the α_k–Ca_v curve converges quickly, which we can see from how close the $\lambda = 100$ and $\lambda \to 0$ curves are. As λ increases, except for very small Ca_v, the curve converges to $\alpha_k = k$. Therefore, under a velocity inlet, large enough λ still produces a preferential flow of $\alpha_k = k$, although if $\alpha_k|_{\lambda=1} > 1$, then there can be an appropriately large λ that allows simultaneous displacement.

The phase diagram under a velocity inlet is given in figures 3(*c*,*d*). The behaviours of preferential flow are different in the three regions divided by the $\alpha_k = k$ and $\alpha_k = 1$ curves. The $\alpha_k = k$ curve is a straight line parallel to the $\log(\lambda)$ axis, while the $\alpha_k = 1$ curve agrees with the findings in a recent work (Gu *et al.* 2021): it becomes invariant

https://doi.org/10.1017/jfm.2022.649 Published online by Cambridge University Press

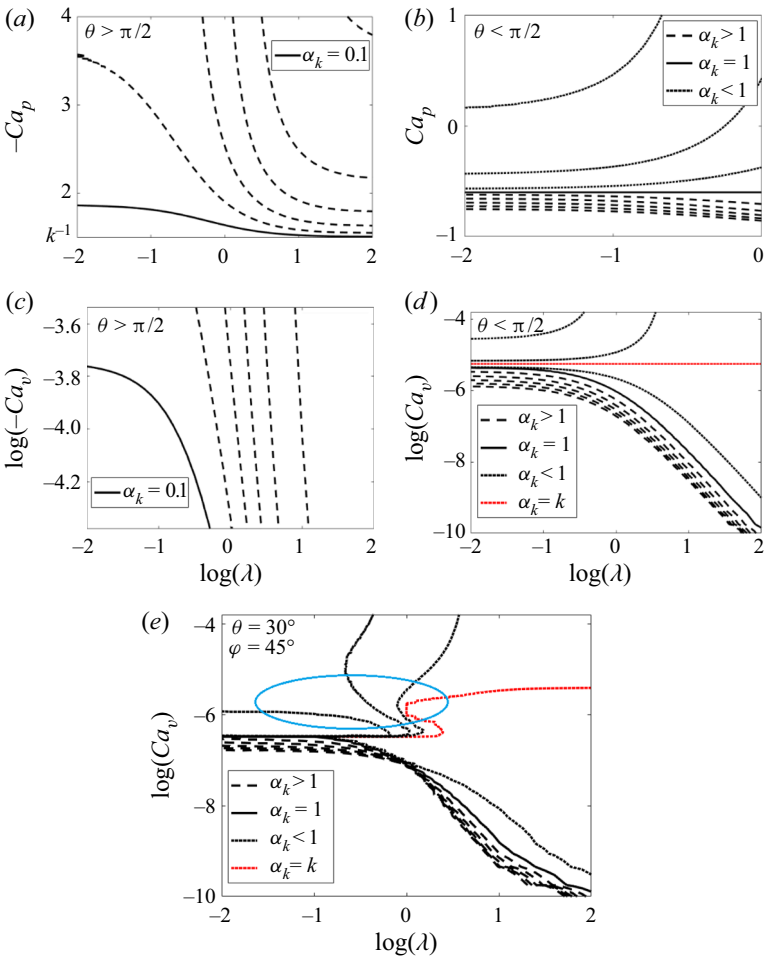


Figure 3. (*a*,*b*,*c*,*d*) The λ–Ca phase diagrams for the preferential flow in the pore doublet, illustrated through the contour lines of α_k: (*a*,*b*) under a pressure inlet at $\theta > \pi/2$ and at $\theta < \pi/2$; (*c*,*d*) under a velocity inlet at $\theta > \pi/2$ and at $\theta < \pi/2$. The difference between two adjacent lines at $\theta > \pi/2$ is 0.01, and at $\theta < \pi/2$ it is 0.02. For better illustration, log-log plots are adopted for the velocity inlet, and Ca in the y-axis at $\theta > \pi/2$ is replaced by $-Ca$ so that the log is meaningful and larger pressure or velocity corresponds to larger y in both wetting conditions. (*e*) Similar to (*d*), but in the dual-permeability porous media at $\theta = 30°$. The difference between two adjacent lines is 0.02. The blue ellipse indicates the abnormal region where the curves bend towards the left compared to the pore doublet case.

in λ at small λ, and turns linear with a negative slope at large λ. We find here that this feature applies not only to the $\alpha_k = 1$ curve in the water-wet condition, as concluded in the previous work, but to all values of α_k and in all wetting conditions. The invariance at small λ is because the whole α_k–Ca_v curve converges quickly with decreasing λ, as shown in figures 3(*c*,*d*), and the linearity at large λ can be deduced mathematically. Different from the case under a pressure inlet, there is no general convergence at large λ. Therefore, the state of preferential flow is no longer determined primarily by Ca_v, but λ plays a crucial role as well. There is still an upper bound of Ca_v beyond which preferential flow cannot be prevented, but for any Ca_v within the bound, there is a λ to achieve simultaneous arrival.

https://doi.org/10.1017/jfm.2022.649 Published online by Cambridge University Press

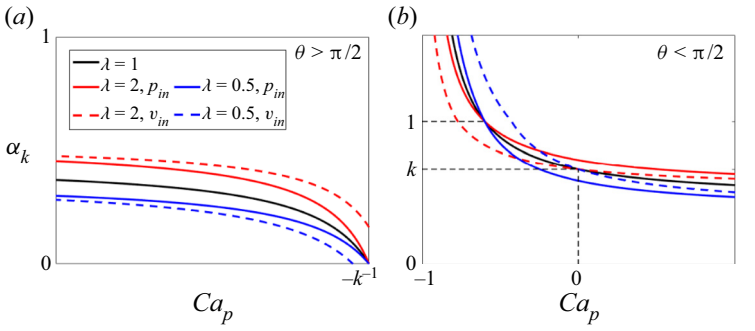


Figure 4. Comparison between the pressure and velocity inlets on the impact of λ on α_k at (*a*) $\theta > \pi/2$, (*b*) $\theta < \pi/2$. For the velocity inlet, the *x*-axis is the equivalent Ca_p at $\lambda = 1$.

A more straightforward comparison can be made between the two boundary conditions by putting them in the same figure. This needs some additional treatments since Ca_v and Ca_p are not comparable directly. Note that the two boundary conditions are equivalent when $\lambda = 1$, so we plot the results from a velocity inlet with Ca_p being the *x*-axis, in the sense that they correspond to the equivalent Ca_v when $\lambda = 1$. The α_k–Ca_v relation at different λ and under different boundary conditions is illustrated in figure 4. The physical meaning of different curves at fixed Ca_p is that we keep the inlet velocity or pressure constant while changing λ from the same $\lambda = 1$ case. We already know that the impact of λ on preferential flow under different boundary conditions can be qualitatively different from separate phase diagrams. Here, we emphasize the difference between boundary conditions even when qualitatively, λ behaves the same. For a water-wet condition, at small Ca_p above the simultaneous point, and for an oil-wet condition at all Ca_p, the impacts of λ on preferential flow are the same under either boundary, but have a stronger impact under a velocity boundary. For a water-wet condition, at large Ca_p under the spontaneous imbibition point, the impact is stronger under a pressure boundary. The difference in α_k between boundary conditions is especially large near the simultaneous point, indicating that the strategy to tune the preferential flow must take the real boundary conditions into account.

Up to this point, we have given a full phase diagram for the pore doublet model that includes the impact of viscosity ratio, capillary number, wetting conditions and boundary conditions. We add a further note about the impact of the wetting conditions here. The preferential flow behaves distinctively differently for water-wet and oil-wet conditions, and that sums up the wettability impact for the pore doublet model because the value of the contact angle has no influence after being scaled in Ca_v and Ca_p. With the other three factors fixed, α_k is always lower for an oil-wet condition as the limit at a large pressure or velocity is the same for both wetting conditions, but the monotonicity is the opposite.

Although it is expected that the phase diagram obtained from a pore doublet is hardly applicable to complex porous media directly, it works quite well qualitatively after two major corrections. The phase diagrams obtained from porous media show high resemblance to those in figures 3(*a–d*), and here we focus mainly on the differences.

The pressure inlet is considered at first. Under the periodically alternating pattern of θ and $\theta + \varphi$, the interface velocity is a weighted harmonic average of the velocity in the homogeneous θ and $\theta + \varphi$ cases. The resulting $\alpha_k - Ca_p$ curve should also be between the two homogeneous cases. Therefore, if both θ and $\theta + \varphi$ are water-wet or oil-wet, then the curve in between also behaves as in the water-wet or oil-wet pore doublet model.

https://doi.org/10.1017/jfm.2022.649 Published online by Cambridge University Press

There is another possibility, that θ is water-wet but $\theta + \varphi$ is oil-wet. As the harmonic average is dominated by the smaller value, we expect that the α_k–Ca_p curve is dominated by the homogeneous $\theta + \varphi$ curve. Both scenarios are validated by simulations. This finding also implies a general principle of the impact of wettability heterogeneity. The dominance of $\theta + \varphi$ is remarkable since it accounts for only 20 % of the total length. Therefore, for a pressure inlet, the critical contact angle that divides the preferential flow behaviours from water-wet to oil-wet is not $\theta = 90^\circ$ but very close to $\theta + \varphi = 90^\circ$. With this correction, the phase diagram for the porous media behaves just like that for the pore doublet under a pressure inlet.

For the velocity inlet, the other correction is needed when Ca_v is small in water-wet conditions, shown in the circled area in figure 3(*e*). Compared to the pore doublet phase diagram, the curves bend towards the left here. The physical meaning is that decreasing Ca_v here decreases α_k as well, unlike in the pore doublet, where α_k increases monotonically with decreasing Ca_v for the water-wet condition. This is somewhat anti-intuitive because a smaller Ca_v means the dominance of capillary force. In the homogeneous case, the capillary driving force is stronger in the narrower channel, so that there forms such a monotonicity. In the simplified model with alternating contact angles, the average capillary driving force is still stronger in the narrower channel, but the monotonicity is lost. By tracking the positions of interfaces during displacement, we find that this is caused by the interaction of the channels, which is distinctive to the velocity inlet because under a pressure inlet, the interface velocity in one channel is not affected by the other. This violation of monotonicity has two prerequisites. First, the narrower channel should dominate when the interfaces in both channels are at θ, but when the interfaces in both channels are at $\theta + \varphi$, the capillary force is weakened so that the wider channel dominates. This requires Ca_v to be not extremely low. Second, when the interface in the narrower channel is at $\theta + \varphi$ and that in the wider channel is at θ, the interface in the narrower channel moves backwards because the corresponding pressure difference is negative. This requires Ca_v to be low enough. As a result, within the certain region where the two prerequisites are met, although the capillary force in the narrower channel is always greater when the interfaces in both channels are at θ or $\theta + \varphi$, the interface in the narrower channel stays at $\theta + \varphi$ much longer than the percentage of length implies, leading to a smaller capillary force on average. Other than this abnormal region, the rest of the phase diagram is consistent with the pore doublet case. The above observations on the dual-permeability media, including the two major differences and the similarity, are not only obtained from the simplified model but also validated qualitatively by our LBM simulations.

We add one more note on the simplified model of dual-permeability media. In figure 1(*c*), it is explained how a flow path with pore–throat junctions can be reduced to a single channel with an alternating pattern of heterogeneous contact angles. By reducing the disordered permeable media to a pore doublet, we assume further that the number of flow paths in different layers of permeability is the same, which is not always true. Consider an additional variable that describes the ratio of flow paths between two layers. Under a pressure inlet, it has little impact because the displacement in each channel is independent. Under a velocity inlet, a higher ratio of the high-permeability layer will decrease the pressure difference. As a result, the phase diagram may shift quantitatively, but all the qualitative features remain. We deduce further that as long as the flow in the horizontal direction dominates, and the range of φ is not too large, the qualitative results can be extended to more complicated dual media because after the simplifying treatment, essentially the same governing equations are solved with similar physical settings.

https://doi.org/10.1017/jfm.2022.649 Published online by Cambridge University Press

4. Conclusions

In summary, we have obtained a complete phase diagram for preferential flow that captures the impacts of viscosity ratio, capillary number, wetting conditions and boundaries for a general dual-permeable medium. To eliminate the preferential flow fully, the media need be effectively water-wet in the sense that $\theta + \varphi < 90^\circ$. Under a pressure inlet, only the capillary number (the external pressure and the capillary pressure) needs to be tuned, while under a velocity inlet, the viscosity ratio also becomes significant. We would like to note further that our treatment of simplifying the converging–diverging feature of permeable media to an alternating pattern of heterogeneous contact angles is proved to be effective and may be applicable to other studies on disordered media.

Funding. This work is funded by the National Key R&D Program of China (no. 2019YFA0708704), NSF grant of China (no. U1837602) and the Tsinghua University Initiative Scientific Research Program for financial support.

Declaration of interests. The authors declare that they have no known competing financial interests or personal relationships that could have appeared to influence the work reported in this paper.

Author ORCIDs.
Moran Wang https://orcid.org/0000-0002-0112-5150.

Author contributions. M.W. conceived and promoted this work. F.L. performed the simulations and analysis. F.L. wrote the paper, and M.W. gave revisions to the text.

Appendix A

A short introduction of the two-phase LBM is given in this appendix. All simulations are performed on a D2Q9 lattice. The lattice velocity is given by

$$\boldsymbol{e_i} = \begin{cases} (0,0), & i = 1, \\ [\sin(\theta_i), \cos(\theta_i)], & i = 2,4,6,8, \\ [\sin(\theta_i), \cos(\theta_i)]\sqrt{2}, & i = 3,5,7,9, \end{cases} \tag{A1}$$

where $\theta_i = (4-i)\pi/4$. The colour-gradient LBM solves for the evolution of distribution functions

$$f_i^{(k)}(\boldsymbol{x} + \boldsymbol{e_i}\,\Delta t, t + \Delta t) - f_i^{(k)}(\boldsymbol{x}, t) = \Omega_i^{(k)}(f_i^{(k)}(\boldsymbol{x}, t)) + F_i, \tag{A2}$$

where $f_i^{(k)}(\boldsymbol{x}, t)$ is the distribution function of the kth phase in the ith direction at position $\boldsymbol{x}$ and time t, Δt is the time step, $\Omega_i^{(k)}(f_i^{(k)}(\boldsymbol{x}, t))$ is the collision term, and F_i is the source term related to body force. The distribution functions are related to the macroscopic density ρ and velocity $\boldsymbol{v}$ as

$$\rho^{(k)} = \sum_i f_i^{(k)}, \quad \rho = \sum_k \rho^{(k)}, \quad \rho\boldsymbol{v} = \sum_k \sum_i f_i^{(k)} \boldsymbol{e_i}. \tag{A3a–c}$$

The Bhatnagar–Gross–Krook (BGK) collision term is adopted in this work:

$$\Omega_i^{(k)}(f_i^{(k)}(\boldsymbol{x}, t)) = -\frac{1}{\tau}\left[f_i(\boldsymbol{x}, t) - f_i^{eq}(\boldsymbol{x}, t)\right], \tag{A4}$$

https://doi.org/10.1017/jfm.2022.649 Published online by Cambridge University Press

where τ is the relaxation time, related to the viscosity as $\nu = (\Delta x/\Delta t)^2(\tau - \Delta t/2)/3$, and $f_i^{eq}(\boldsymbol{x}, t)$ is the equilibrium distribution function, calculated as

$$f_i^{(k),eq}(\boldsymbol{x}, t) = \rho^k \left(C_i + \omega_i \left[\frac{3(\boldsymbol{e_i} \cdot \boldsymbol{v})}{c^2} + \frac{9(\boldsymbol{e_i} \cdot \boldsymbol{v})^2}{2c^4} - \frac{3(\boldsymbol{v} \cdot \boldsymbol{v})}{2c^2} \right] \right), \tag{A5}$$

$$C_i = \begin{cases} \alpha^{(k)}, & i = 0, \\ \dfrac{1 - \alpha^{(k)}}{5}, & i = 1, 2, 3, 4, \\ \dfrac{1 - \alpha^{(k)}}{20}, & i = 5, 6, 7, 8, \end{cases} \tag{A6}$$

$$\omega_i = \begin{cases} \dfrac{4}{9}, & i = 0, \\ \dfrac{1}{9}, & i = 1, 2, 3, 4, \\ \dfrac{1}{36}, & i = 5, 6, 7, 8, \end{cases} \tag{A7}$$

where $\alpha^{(k)}$ is a parameter chosen to be 0.6 in this work. Body force $\boldsymbol{F}$ should be applied at the interface to achieve surface tension σ:

$$\boldsymbol{F} = -\tfrac{1}{2}\sigma\kappa\, \nabla\rho^N, \tag{A8}$$

$$\rho^N(\boldsymbol{x}, t) = \frac{\rho^{(1)}(\boldsymbol{x}, t) - \rho^{(2)}(\boldsymbol{x}, t)}{\rho^{(1)}(\boldsymbol{x}, t) + \rho^{(2)}(\boldsymbol{x}, t)}, \tag{A9}$$

$$\kappa = -[(\boldsymbol{I} - \boldsymbol{n} \otimes \boldsymbol{n}) \cdot \nabla] \cdot \boldsymbol{n}, \tag{A10}$$

$$\boldsymbol{n} = -\nabla\rho^N / |\nabla\rho^N|. \tag{A11}$$

Here, the contact angle is applied with a geometrical method. The body force is related to the source term as

$$F_i = \omega_i \left(1 - \frac{1}{2\tau} \right) [3(\boldsymbol{e_i} - \boldsymbol{v}^*) + 9(\boldsymbol{e_i} \cdot \boldsymbol{v}^*)\boldsymbol{e_i}] \cdot \boldsymbol{F}, \tag{A12}$$

$$\boldsymbol{v}^* = \frac{1}{\rho} \left(\sum_i f_i \boldsymbol{e_i} + \frac{1}{2}\boldsymbol{F} \right). \tag{A13}$$

After the BGK collision, a recolouring step is applied to enhance the separation of phases:

$$f_i^{(1)} = \frac{\rho^{(1)}}{\rho} f_i^* + \beta \frac{\rho^{(1)}\rho^{(2)}}{\rho^2} \cos(\lambda_i) \sum_k f_i^{(k),eq}(\rho^{(k)}, 0, \alpha^{(k)}), \tag{A14}$$

$$f_i^{(2)} = \frac{\rho^{(2)}}{\rho} f_i^* + \beta \frac{\rho^{(1)}\rho^{(2)}}{\rho^2} \cos(\lambda_i) \sum_k f_i^{(k),eq}(\rho^{(k)}, 0, \alpha^{(k)}), \tag{A15}$$

where $\cos(\lambda_i) = \boldsymbol{e_i} \cdot \nabla\rho^N / (|\boldsymbol{e_i}|\, |\nabla\rho^N)|$.

https://doi.org/10.1017/jfm.2022.649 Published online by Cambridge University Press

References

Aker, E., Måløy, K.J. & Hansen, A. 2000 Viscous stabilization of 2D drainage displacements with trapping. *Phys. Rev. Lett.* **84** (20), 4589.

Al-Housseiny, T.T., Hernandez, J. & Stone, H.A. 2014 Preferential flow penetration in a network of identical channels. *Phys. Fluids* **26** (4), 042110.

Babchin, A., Brailovsky, I., Gordon, P. & Sivashinsky, G. 2008 Fingering instability in immiscible displacement. *Phys. Rev.* E **77** (2), 026301.

Bahadori, A. 2018 *Fundamentals of Enhanced Oil and Gas Recovery from Conventional and Unconventional Reservoirs*. Gulf Professional.

Chatzis, I. & Dullien, F.A.L. 1983 Dynamic immiscible displacement mechanisms in pore doublets: theory versus experiment. *J. Colloid Interface Sci.* **91** (1), 199–222.

Chen, G. & Neuman, S.P 1996 Wetting front instability in randomly stratified soils. *Phys. Fluids* **8** (2), 353–369.

Cieplak, M. & Robbins, M.O. 1988 Dynamical transition in quasistatic fluid invasion in porous media. *Phys. Rev. Lett.* **60** (20), 2042.

Cottin, C., Bodiguel, H. & Colin, A. 2010 Drainage in two-dimensional porous media: from capillary fingering to viscous flow. *Phys. Rev.* E **82** (4), 046315.

Ferer, M., Ji, C., Bromhal, G.S., Cook, J., Ahmadi, G. & Smith, D.H. 2004 Crossover from capillary fingering to viscous fingering for immiscible unstable flow: experiment and modeling. *Phys. Rev.* E **70** (1), 016303.

Good, S.P., Noone, D. & Bowen, G. 2015 Hydrologic connectivity constrains partitioning of global terrestrial water fluxes. *Science* **349** (6244), 175–177.

Gu, Q., Liu, H. & Wu, L. 2021 Preferential imbibition in a dual-permeability pore network. *J. Fluid Mech.* **915**, A138.

Guo, H., Song, K. & Hilfer, R. 2020 A critical review of capillary number and its application in enhanced oil recovery. In *SPE Improved Oil Recovery Conference*. OnePetro.

Hewitt, D.R., Neufeld, J.A. & Lister, J.R. 2014 High Rayleigh number convection in a porous medium containing a thin low-permeability layer. *J. Fluid Mech.* **756**, 844–869.

Holtzman, R. & Segre, E. 2015 Wettability stabilizes fluid invasion into porous media via nonlocal, cooperative pore filling. *Phys. Rev. Lett.* **115** (16), 164501.

Huppert, H.E. & Neufeld, J.A. 2014 The fluid mechanics of carbon dioxide sequestration. *Annu. Rev. Fluid Mech.* **46**, 255–272.

Jensen, O.E. & Chernyavsky, I.L. 2019 Blood flow and transport in the human placenta. *Annu. Rev. Fluid Mech.* **51**, 25–47.

Khayamyan, S., Lundström, T.S. & Gustavsson, L.H. 2014 Experimental investigation of transitional flow in porous media with usage of a pore doublet model. *Transp. Porous Med.* **101** (2), 333–348.

Lenormand, R., Touboul, E. & Zarcone, C. 1988 Numerical models and experiments on immiscible displacements in porous media. *J. Fluid Mech.* **189** (1), 165–187.

Lenormand, R. & Zarcone, C. 1985 Invasion percolation in an etched network: measurement of a fractal dimension. *Phys. Rev. Lett.* **54** (20), 2226.

Liu, F. & Wang, M. 2022*a* Trapping patterns during capillary displacements in disordered media. *J. Fluid Mech.* **933**, A52.

Liu, F. & Wang, M. 2022*b* Wettability effects on mobilization of ganglia during displacement. *Intl J. Mech. Sci.* **215**, 106933.

Måløy, K.J., Feder, J. & Jøssang, T. 1985 Viscous fingering fractals in porous media. *Phys. Rev. Lett.* **55** (24), 2688.

Moore, T.F. & Slobod, R.L. 1955 Displacement of oil by water-effect of wettability, rate, and viscosity on recovery. In *Fall meeting of the petroleum branch of AIME*, SPE-502-G. OnePetro.

Odier, C., Levaché, B., Santanach-Carreras, E. & Bartolo, D. 2017 Forced imbibition in porous media: a fourfold scenario. *Phys. Rev. Lett.* **119** (20), 208005.

Oliveira, L.I., Demond, A.H., Abriola, L.M. & Goovaerts, P. 2006 Simulation of solute transport in a heterogeneous vadose zone describing the hydraulic properties using a multistep stochastic approach. *Water Resour. Res.* **42** (5), W05420.

Payatakes, A.C. 1982 Dynamics of oil ganglia during immiscible displacement in water-wet porous media. *Annu. Rev. Fluid Mech.* **14** (1), 365–393.

Phillips, O.M. 2009 *Geological Fluid Dynamics: Sub-surface Flow and Reactions*. Cambridge University Press.

Primkulov, B.K., Pahlavan, A.A., Fu, X., Zhao, B., MacMinn, C.W. & Juanes, R. 2021 Wettability and Lenormand's diagram. *J. Fluid Mech.* **923**, A34.

https://doi.org/10.1017/jfm.2022.649 Published online by Cambridge University Press

SORBIE, K.S., WU, Y.Z. & MCDOUGALL, S.R. 1995 The extended Washburn equation and its application to the oil/water pore doublet problem. *J. Colloid Interface Sci.* **174** (2), 289–301.

TARTAKOVSKY, A.M., NEUMAN, S.P. & LENHARD, R.J. 2003 Immiscible front evolution in randomly heterogeneous porous media. *Phys. Fluids* **15** (11), 3331–3341.

TROJER, M., SZULCZEWSKI, M.L. & JUANES, R. 2015 Stabilizing fluid–fluid displacements in porous media through wettability alteration. *Phys. Rev. Appl.* **3** (5), 054008.

ZHANG, C., OOSTROM, M., WIETSMA, T.W., GRATE, J.W. & WARNER, M.G. 2011 Influence of viscous and capillary forces on immiscible fluid displacement: pore-scale experimental study in a water-wet micromodel demonstrating viscous and capillary fingering. *Energy Fuels* **25** (8), 3493–3505.

ZHENG, J., CHEN, Z., XIE, C., WANG, Z., LEI, Z., JU, Y. & WANG, M. 2018 Characterization of spontaneous imbibition dynamics in irregular channels by mesoscopic modeling. *Comput. Fluids* **168**, 21–31.

https://doi.org/10.1017/jfm.2022.649 Published online by Cambridge University Press